Seismological Studies at Parkfield IX: Fault-Zone Imaging Using Guided Wave Attenuation

by V. A. Korneev, R. M. Nadeau, and T. V. McEvilly

Abstract   Numerical modeling studies and a growing number of observations have argued for the propagation of fault-zone guided waves (FZGWs) within a San Andreas Fault (SAF) zone that is 100–200 m wide at seismogenic depths and with 20%–40% lower shear-wave velocity than the adjacent unfaulted rock. Thousands of microearthquakes have been recorded since 1987 by the borehole High-Resolution Seismic Network at Parkfield, California, and they provide a comprehensive data set for characterizing wave propagation in the SAF zone. Using microearthquakes we confirm that FZGWs at Parkfield are generated within the fault zone (FZ) and that they are most prominent late in the coda of S. Numerical waveform modeling and guided-wave amplitude tomographic inversion show clearly that FZGWs are significantly less attenuated in a well-defined region of the FZ. This region plunges to the northwest along the northwest boundary of the region of highest moment release and separates locked and slipping sections of the SAF at depth, as determined independently from geodesy, seismicity, and the recurrence rates of characteristically repeating microearthquakes. We interpret this localized zone of strong FZGW propagation to be the northwest edge of the M 6 asperity at Parkfield. The mechanism for low FZGW attenuation in the zone is possibly due to dewatering by fracture closure and/or fault-normal compression or changes in fracture orientation due to a complex stress or strain field at the boundary between creeping and locked zones of the SAF.

Introduction

Intriguing claims have been made from a growing body of observations and from modeling studies about the imaging power of fault-zone guided waves (FZGWs) for characterizing space and time-dependent properties and processes within the central cores of active fault zones (FZs). FZGWs were originally identified early by Aki and coworkers (e.g., Leary *et al.*, 1985; Li *et al.*, 1990) in active-source surface-to-borehole studies and later from seismograms recorded in or near the FZs from local earthquakes. These waves are most visible for sources within a well-developed FZ and with receivers located within the same FZ segment (Li *et al.*, 1994, 1997). They also appear to be generated by off-fault surface sources (Korneev *et al.*, 2000). FZGWs are trapped by material in the fault that has a lower seismic-wave velocity than the surrounding, more intact rock. The low-velocity nature of the San Andreas Fault (SAF) zone core has long been recognized (see Feng and McEvilly [1983], for a summary of early velocity models). FZGWs at Parkfield are seen in the coda of both P and S waves, but they are generally stronger in the S-wave coda, with large amplitudes in some cases arriving as late as twice the S-wave travel time. They usually exhibit lower frequency content than the direct P or S waves, and in many cases they appear to be dispersive.

There are compelling reasons to study the FZGW phenomenon. The most general reason is their potential for defining the structure of the active FZ at depth, which includes features that bound rupture extent in large earthquakes (segmentation boundaries, gaps, streaks, or asperities) and may be evident in FZGW propagation characteristics. Detection of transient or systematic changes within the fault core through successful FZGW imaging in four dimensions is also a potentially powerful monitoring method (Li *et al.*, 1998). In this study, we focus on the structural and wave propagation aspects of the FZ using properties of FZGW propagation from thousands of microearthquake sources.

Thicknesses of the central regions of faults (fault core) can be defined by the geometry of velocity discontinuities across the FZ and by the dominant seismic wavelength. The SAF at Parkfield has an approximate core thickness of 100–300 m (Korneev *et. al*, 2000). Inversion of P- and S-phase arrivals allows imaging of macroscale properties in the vicinity of FZs with lateral resolution of about 5 km; however, the characteristic width of the most active region of faults appears to be on the order of a few hundred meters or less. The lower seismic velocities in the cores of FZs causes propagation of the first-arriving P and S phases to occur primarily

outside of the central low-velocity zone. As a result, the resolution of first-arrival body-wave inversions for FZ structure is severely limited.

In contrast, FZGW propagation takes place almost entirely within the central low-velocity region of the FZ, allowing for sampling and mapping of inner FZ properties in detail. In this study we use data from just two stations located close to the fault to obtain structural images with 0.5 km resolution, about an order of magnitude better than the resolution achieved using travel-time tomography with many more seismic stations.

The Parkfield Data Set

One of the best data sets available for characterizing the spatial and temporal properties of FZGWs is the accumulation of microearthquake and Vibroseis recordings from the High-Resolution Seismic Network (HRSN) at Parkfield, California (Fig. 1). The current network consists of 13 three-component deep (~200 m) borehole seismometers. FZGW data for this study come from 2 stations of an original 10-station network (see Karageorgi et al., [1992], for a description of the original 10-station network and Vibroseis monitoring details) spanning the SAF.

HRSN data are unique. The very low noise environment at recording depths of 200 m or more allows detection of microearthquakes as small as M −1 and recording of seismic frequencies greater than 100 Hz. Since is installation in 1987, the HRSN has recorded more than 6000 microearthquakes along a 25-km stretch of the SAF. Furthermore, more than 60% of these events are members of about 300 similar-event clusters and sequences of repeating, virtually identical earthquakes exhibiting very small source dimensions (Nadeau et al., 1994, 1995; Nadeau and McEvilly, 1997). These thousands of microearthquakes along the FZ, with similar strike-slip mechanisms, allow construction of record sections or common-station gathers of seismograms for swaths of sources in almost any desired geometry on the fault plane and for any instrument component. In effect, the slipping FZ is covered with point sources that are available for 3D imaging investigations of regional FZ structure at high spatial resolution. As an unexpected bonus, the fourth dimension, time, is accessible by virtue of the widely distributed repeating sources in the sequences of characteristic microearthquakes. At M ~0, these sequences repeat with recurrence intervals of less than 1 year (see figure 9 in Nadeau and McEvilly [1997], or figure 11 in Nadeau and Johnson [1998]), providing potentially important data for monitoring.

In this study we define the nature of wave propagation within a narrowly defined FZ core (approximately 200 min width) to image the structural characteristics of the central FZ in detail. Our ultimate goal is to understand better the nature of wave propagation in the SAF zone at Parkfield and explore the utility of guided waves for many potentially important applications.
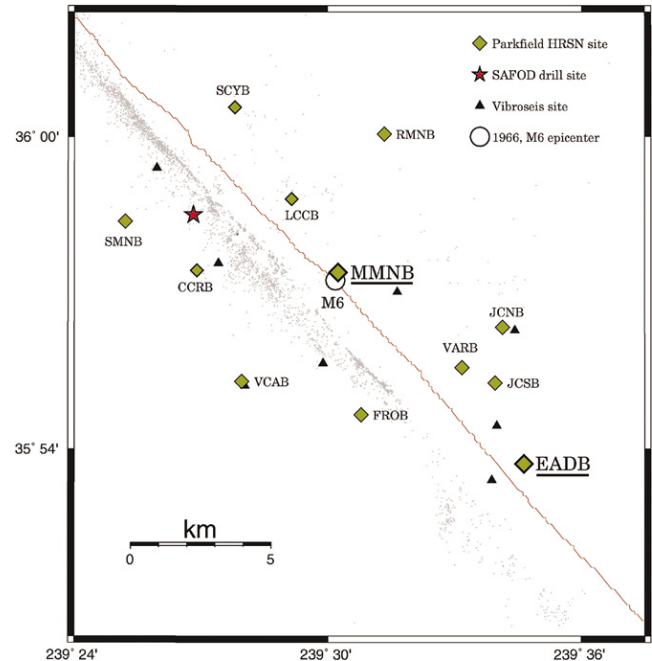

Figure 1. Map of the borehole 13, three-component station High-Resolution Seismic Network (HRSN) at Parkfield subsequent to its expansion in 2000–2001. Seismicity used in this study was recorded between January 1987 and July 1998 on the original 10 stations of the HRSN (i.e., excluding SCYB, LCCB, and CCRB), and its relocated epicenters are shown as gray points. Station GHIB is off the map approximately 8 km southeast of station EADB along the San Andreas Fault trace. In this article we use data recorded at stations MMNB and EADB. Also shown are eight source points of the Parkfield Vibroseis experiment, the proposed drilling site of the San Andreas Fault Observatory at depth (SAFOD), and the epicenter of the 1966 M 6 earthquake, which is used as the origin of the coordinate system.

Inversion of FZGWs at Parkfield

Anomalous wave propagation associated with the FZ at Parkfield has been studied previously. Li et al. (1990) and Ben-Zion and Malin (1991) identified the distinctive late S-coda arrivals from Parkfield earthquakes as propagation of trapped and head-wave energy, respectively, along a low-velocity FZ. They proceeded to model them as SH propagation in a 2D structure consisting of a homogeneous low-velocity plane wave guide bounded by sharp interfaces.

Our initial step in this investigation was to look at the nature of FZGWs with respect to hypocenter location and receiver position, in order to map any obvious features in the spatial relationship of source and receiver. The two stations closest to the FZ (EADB and MMNB, about 500 and 100 m from the fault, respectively; see Fig. 1) provide an appropriate geometry for recording FZGWs. This geometry also provides a "reversed" profile of sources along the fault using receiver gathers of microearthquake traces. We illus-

trate this form of data presentation in Figure 2 with record sections for a collection of more than 500 sources taken along the fault segment at a depth range of 3.3–3.8 km. Waveform coherence is strong along the profile because a common strike-slip mechanism dominates the mode of slip on the fault. This allows stacking of waveforms from nearby sources for an enhanced signal-to-noise ratio. The frequency content of typical waveforms that contain strong FZGWs is also shown in the figure. Note the low-frequency content (around 4 Hz) that characterizes the FZGW arrival. In contrast, the direct *P*- and *S*-wave energy is relatively small.

Several first-order observations can be made. Large-amplitude FZGWs are clearly seen in the coda of *S* waves. They exhibit lower frequency content than the direct body waves and some dispersion, with higher frequencies showing lower group velocities. The strong energy late in the coda of *S*, however, is not present for all sources in the gathers, and its strength relative to the direct *P* and *S* waves varies with source location along the FZ. FZGW energy is strongest on the MMNB section for sources southeast of -3 km along the fault, while at station EADB, much weaker FZGWs are seen from the same sources. Much stronger FZGW arrivals are observed at EADB, however, for sources farther to the northwest at along-fault coordinates greater then zero.

To characterize further the spatial distribution of FZGW source strength as seen at MMNB and EADB, we extended the analysis to all sources within the full depth and length range of the study zone and defined a FZGW strength in an interval within the *S*-coda, relative to the direct *S* wave. Sources used were earthquakes occurring within 1 km of a best-fit plane to the overall seismicity. We also used only events having *S*-wave amplitudes greater than 11 times the pre-event background signal level in the 2.5–5.5-Hz bandwidth. Ratios of three-component spectral amplitudes in the 2.5–5.5-Hz band were computed for windows nominally 1- and 4-sec long beginning at 1.7 and 2.3 times the *P*-wave travel time, for the direct *S* and the FZGW arrivals, respectively. Figure 2 illustrates how the moveouts of the *S* and FZGW phase arrivals are comparable, allowing us to apply this simple windowing scheme to the entire data set. The results for stations MMNB and EADB are shown in Figure 3. Ratios were normalized to an average value of 0.5 for plotting, and the ratios of 0.5 and 0.7 differentiate the three categories of FZGW strength shown in the figure.

We observe that strong FZGWs occur at a given station along the fault only when their source-station paths intersect the narrow transition zone of the orange to blue color change in Figure 3. To define more quantitatively this zone, we performed a tomographic inversion based on normalized FZGW/*S* amplitude ratios. We inverted for seismic attenuation of the FZGW phase because the systematic variations in FZGW amplitudes are the most prominent feature of their propagation and because attenuation coefficients lend themselves more readily to the interpretation of rock properties from propagation effects. The sources for our inversion are naturally occurring earthquakes with varying magnitudes

and frequency content. To compensate for these variations, the three-component vector amplitude ratios of windowed FZGW to *S*-wave arrivals for each event determined within a low-frequency band (2.5–5.5 Hz, well below the source corner of these M -1 to 1.5 events) are used. The algorithm of the FZGW inversion is described in the Appendix. We used the following model to describe the amplitudes of guided waves in the fault:

$$ U_{ij} = A_j M_i \frac{\kappa(\theta_{ij})}{\sqrt{r_{ij}}} \exp\left(- \sum_n \alpha_n r_{ijn}\right), \qquad (1) $$

where U_{ij} is the recorded amplitude for source i and receiver j, A_j is the station-specific local guided-wave amplification factor, M_i is the seismic moment of the event and $\kappa(\theta_{ij})$ describes the source radiation pattern, r_{ij} the total ray length, α_n the attenuation coefficient in region n, and r_{ijn} the partial ray length in that region. The usual attenuation parameter Q was computed after the inversion for attenuation coefficient using the formula

$$ Q_n = \frac{\omega}{2\alpha_n V_s}, \qquad (2) $$

where ω is frequency and V_s is the *S* wave velocity taken from travel-time inversion. Since for the inversion we used guided-wave/*S*-wave amplitude ratios, the seismic moment factors were canceled and the local amplification factors were related to those ratios, as $\bar{A}_j = A_j/A_{Sj}$, where A_{Sj} is a local *S*-wave amplification factor. Radiation patterns for both waves are assumed to be proportional to each other.

Our inversion used a 100 by 30 grid with 0.5-km square pixels, resulting in a 50 by 15 km model grid size. The number of sources used for ray paths into stations MMNB and EADB were 3353 and 1892, respectively. The number of sources used at EADB was smaller, since fewer of the seismograms recorded at this station fulfilled the minimum *S*-phase signal-to-noise ratio criteria of 11. Results of the inversion yielded ratios of guided-wave/*S*-wave amplification factors of $\bar{A}_{MMNB}$ and $\bar{A}_{EADB}$ of 0.21 and 0.7, respectively. Factors responsible for the difference between these values may include the FZ core position with respect to the surface trace of the SAF and an unknown guided-wave amplitude distribution across the fault due to the nodal points configuration of different guided-wave modes. Another factor that affects the ratios is the complex character of *S*-wave energy, which for station EADB propagates as body waves on the low-velocity northeast side and arrives from the southwest high-velocity side of the SAF in the form of head waves.

Results of the full attenuation inversion shown in Figure 4a define a low-attenuation feature that extends from a shallow zone of intense microearthquake activity southeast of MMNB and dips to the northwest through the rupture zones of accelerated $M > 4$ activity occurring in 1992–1994 and through the 1966 M 6 hypocenter. The ray coverage shown
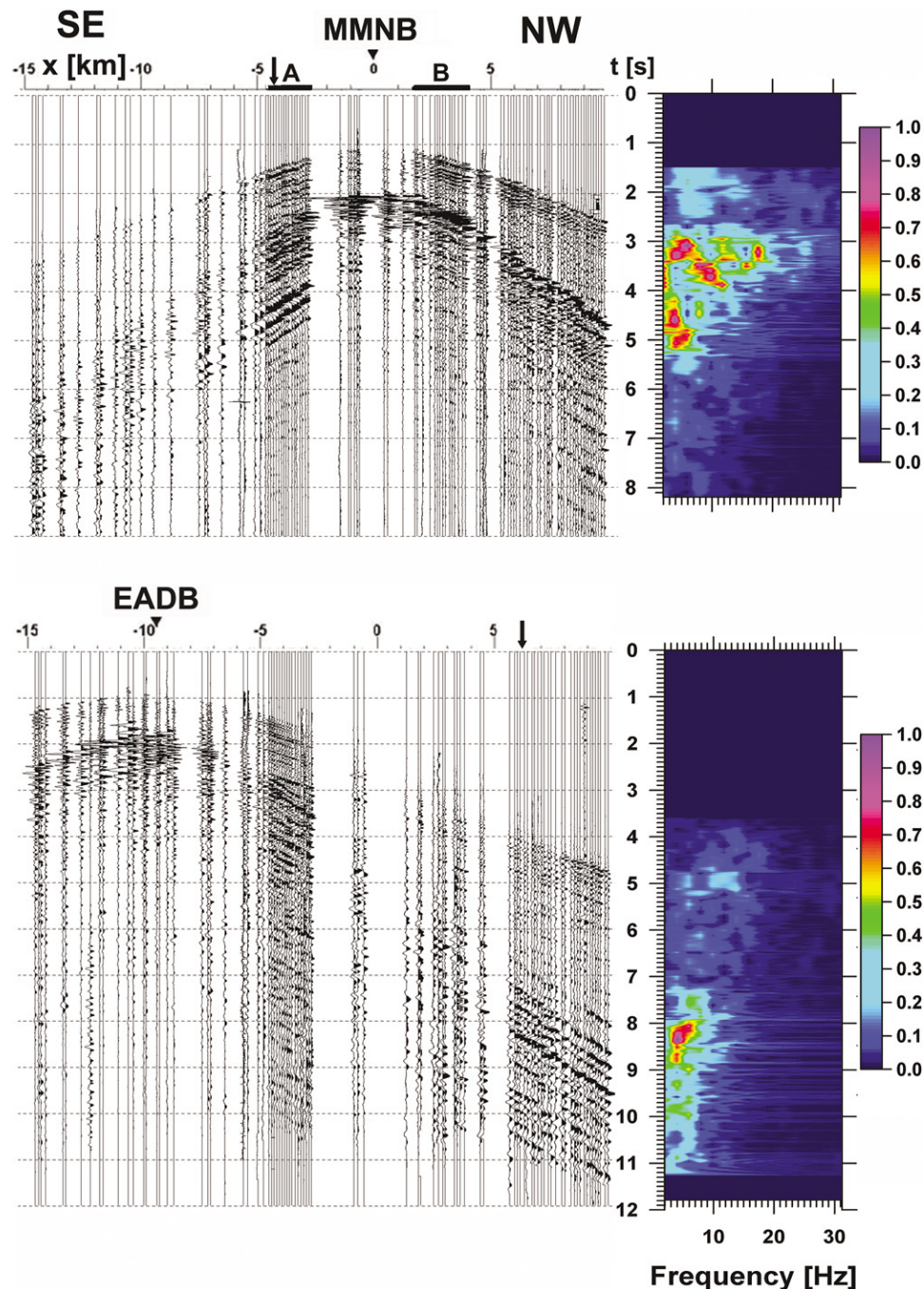
Figure 2. Station gathers and spectral content of microearthquake sources. Left: Record sections or station gathers of horizontal-component seismograms for stations MMNB and EADB, which constitute a reversed profile of sources (all with the same strike-slip mechanisms) in the depth range 3.3–3.8 km along a 25-km stretch of the FZ (the 1966 M 6 epicenter is at 0 km); 102 traces are shown for MMNB, 84 for EADB, having been stacked in 10-m bins from 531 and 351 initial traces, respectively (only 351 of the initial 531 sources produced usable records at the much noisier EADB station). A and B show locations of source profiles used later in the modeling exercise (Fig. 7). FZGWs are clearly evident in the coda of the S wave. Note the systematic spatial variability in the FZGWs. For the sources recorded by MMNB there are strong FZGW arrivals for sources southeast of MMNB, while for sources northwest of MMNB these arrivals are much weaker. However, for the same northwest sources recorded at EADB, the FZGW arrivals are again strong; that is, the same earthquakes do not produce strong FZGWs at both stations. Right: Amplitude spectra for selected traces (arrows on sections) computed for a moving window of 500 msec along the seismograms. Offset distances are -4.5 km for MMNB and 8 km for EADB. Note the very low frequency (3–8 Hz) content of the FZGWs that is not seen in the direct P- and S-wave arrivals. This suggests that the low-frequency FZGW energy is derived from the direct P and/or S phases. We define the low-frequency, late-arriving energy as the FZGW phase in this article.
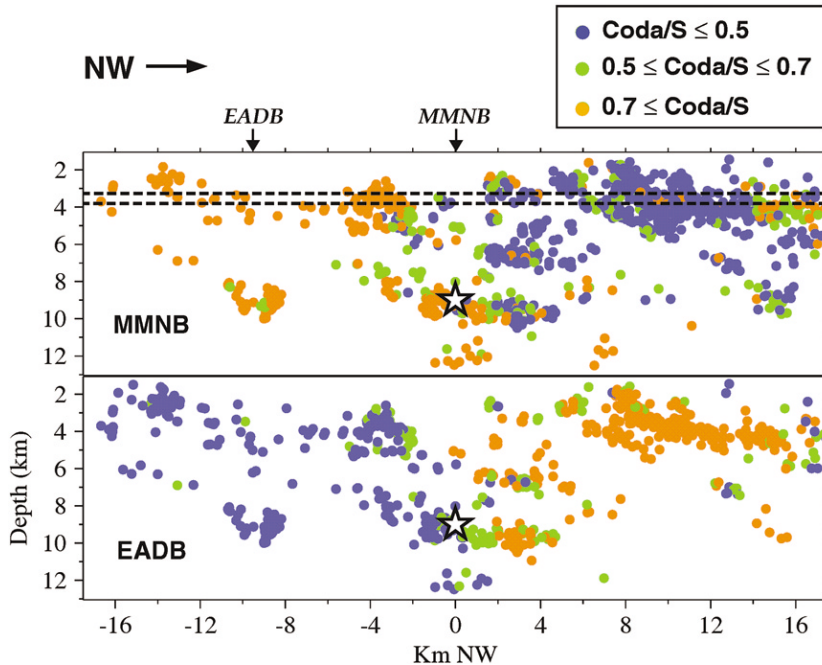
Figure 3. Strength of the FZGW (coda) arrival relative to the direct *S*-wave amplitude for sources along a 35-km segment of the FZ centered at the 1966 epicenter (star) in the 2.5- to 5.5-Hz bandwidth for nominal 4- and 1-sec windows (FZGWs and *S*-waves respectively) positioned relative to the *P*-wave travel time (see text for details). Ratios are normalized to a value of 0.5 and categorized at ratios (1) less than 0.5 (orange filled circles), (2) greater than 0.7 (blue filled circles), and (3) intermediate values shown in green. The upper panel shows data recorded at station MMNB, the lower panel EADB. Note the contrasting dependence on source location of the relative strength of the FZGWs at the two recording sites, with a clear change occurring across and above the hypocentral region of the 1966 *M* 6 event.

on Figure 4b has little correlation with the inversion result. As a test of the robustness of the inversion, we performed an inversion excluding all sources in the central 12 km of the fault segment at all depths. Both inversions showed similar structure and detail in their images. Another series of tests involved declustering and sparse source distributions that reduced the total number of sources by up to 20 times. The resulting images had slightly reduced resolution but retained all the main features.

Modeling FZ Wave Propagation

Properties of the propagating wave field inside and in the vicinity of the FZ are controlled to first order by the velocity, attenuation, and geometry of the wave guide. Two-dimensional numerical modeling studies have been used to illustrate the complexities of wave propagation within a simple plane-parallel low-velocity fault structure (Ben-Zion and Aki, 1990; Ben-Zion and Malin, 1991). Igel *et al.* (1997) explored with finite-difference modeling the effects of irregular FZ geometries and nonuniform material properties. Ben-Zion (1998) presented a comprehensive set of 2D calculations for FZ wave propagation along FZ made up of two homogeneous layers sandwiched between two differing quarter-spaces to illustrate the effects of layer geometry and velocity contrast. More complex modeling, however, is required to allow for full 3D variation of FZ geometry and physical properties (Li *et al.*, 1998, 1999).

In this study, FZGW modeling was based on 2D elastic finite-difference simulations. The main features of the starting model were taken from the tomographic inversion for *P* and *S* velocities from Parkfield microearthquake data (Michelini and McEvilly, 1991) modified using additional earth-

quake data provided by A. Kirkpatrick (personal comm., 2000) and a model for the shallow FZ taken from Korneev *et al.* (2000). We numerically tested the FZ models using both discontinuous and smooth lateral velocity variations. The computed results were compared with data to match arrival times of the body waves and the character of the late-arriving FZGWs. The key features we attempted to generate included the following:

1. Multiple strong arrivals following the direct body waves
2. The arrival time of the main energy in the FZGW
3. The frequency content of FZGWs
4. The relative amplitudes of direct body waves and FZGWs.

We varied the fault width (from 10 to 500 m), sharpness of the boundaries between the FZ and the adjacent media, shape of the FZ, velocity distribution within it, and source positions. The source used was a force couple, striking along the fault.

The modeling comprised two stages. In the first stage we obtained parameters for the reference wave-guide model. In the second stage we looked for a likely cause of the amplitude anomaly. We found that the models containing local velocity variations within the FZ did not provide a good match with the data. Even sharp discontinuous boundaries of velocity anomalies gave little effect on amplitudes. This result is also in agreement with the smooth undisturbed character of FZGW travel times. Only the introduction of an attenuation heterogeneity gave satisfactory results. Therefore, a viable model for simulation of the observed FZGW propagation must include a region of relatively high *Q* (low attenuation) existing exclusively in the narrow zone of large FZGW amplitudes. Anomalous FZ velocity is not required within the large-amplitude zone.
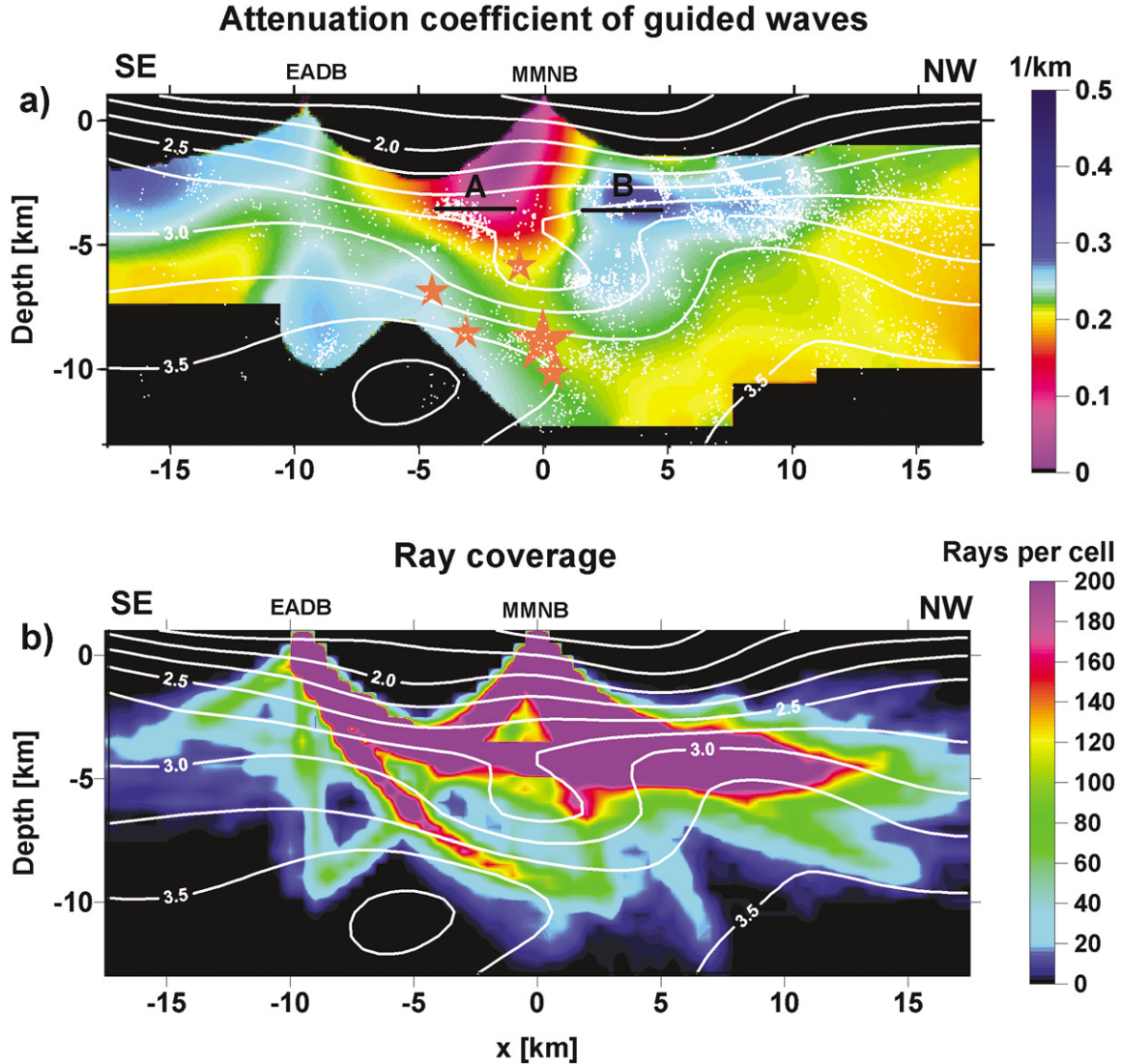
Attenuation coefficient of guided waves

Ray coverage

Figure 4.   (a) Tomographic inversion results of spectral amplitude ratios used in Figure 3 showing the distribution of FZGW attenuation. Contour lines show the *S*-wave velocity model of Michelini and McEvilly as modified with added observations by A. Kirkpatrick (personal comm., 2000). The 1966 *M* 6 hypocenter (largest orange star) and four *M* >4 events occurring between 1992–1994 events (smaller orange stars) are also shown. Line segments A and B represent the source profiles used in modeling (Fig. 7). (b) The density of ray coverage has little spatial correlation with the inversion image.

The resulting model is shown in Figure 5. The model features a strong shallow vertical velocity gradient and a low-velocity FZ with a thickness of 200 m. Tests indicate that deviation of the thickness within 15% of its value also provides a satisfactory match with the data. The velocity in the FZ is half of that on the fast southwest side of the fault. The FZ has discontinuous velocities at its boundaries. The transitional boundaries did not yield the observed FZGW characteristics, a result consistent with those of Ben-Zion and Malin (1991). The velocities shown are representative of those just outside of the narrow FZ and not velocities in the country rock well away from the fault. V_p/V_s is taken to be 2.0 throughout the model, which matches the observed

P, *S*, and FZGW travel times along the FZ. These values are consistent with the tomographic velocity model, which, of course, does not provide the resolution needed for the modeling exercise (the velocity tomography used a fault-normal grid spacing of 1.2 km). For purposes of computational efficiency, we simulated shallow single-borehole recordings for a number of deep sources using source-receiver reciprocity. We computed the wave field for a source at 300 m depth within the FZ for a line of receivers at depth of 7 km, as shown in the figure.

Figure 6 shows results for a 41-element array across the FZ, incorporating the velocity structure in Figure 5 and a high-*Q* fault region (*Q* = 50 versus 10 elsewhere in the FZ)
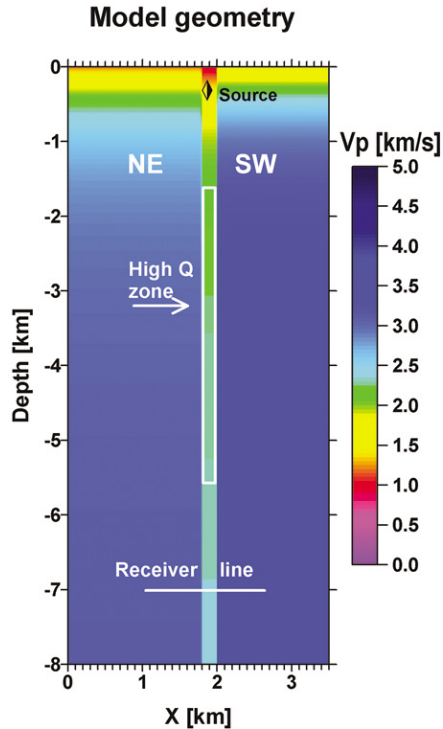
Model geometry

Figure 5. Model geometry used in the finite-difference computation of the wave field within and close to the FZ. V_p is shown, V_s is 0.5 V_p throughout, representative of conditions in the FZ and in the wall rock adjacent to the sharply bounded FZ. The velocity within the 200-m-wide FZ is about 0.5 that in the Salinian wall rock to the southwest. Source and receiver positions are shown, and reciprocity is used to compute the wave field at 300 m depth. The region of anomalously high Q within the FZ is also shown.

Figure 6. Synthetic seismograms using the preferred model of FZGW propagation at Parkfield shown in Figure 5. Data are computed for a 41-element array with 50-m spacing across the FZ at 7-km depth for a source at 300 m depth. The strong low-frequency arrivals late in the coda of both the P and S waves are the modeled FZGWs. The 4-km long high-Q (50, versus 10 elsewhere in the FZ) segment is required to reproduce the observed characteristics of the earthquake data within the FZ.

4 km in depth extent. Material outside of the FZ is less attenuative and has $Q = 200$. This Q model gave us the best match with the observed waveforms. The receiver spacing is 50 m. Fault-normal horizontal and vertical components of particle velocity were generated, and the model velocities have been fine-tuned to match the observed arrival times. These synthetic seismograms display the characteristics of the observed FZGWs, and we use them in further comparisons of the spatial distribution of the guided waves. The multiple-phase character of the direct P and S waves is a result of their propagation along the low-velocity FZ, which can be observed in data on Figure 2. The direct P- and S-wave trains have relatively low amplitudes in and near the FZ, where they arrive as head waves, losing energy due to both refraction and attenuation.

In Figure 7 we show a comparison of synthetic and observed data for a group of horizontal along-fault component seismograms recorded at MMNB, using the selected model of Figure 5 with the Q structure determined from the synthetics in Figure 6. Two profiles for segments A and B (traces, Fig. 2; earthquakes, Fig. 4) represent swaths from shallow earthquakes a few kilometers on either side of sta-
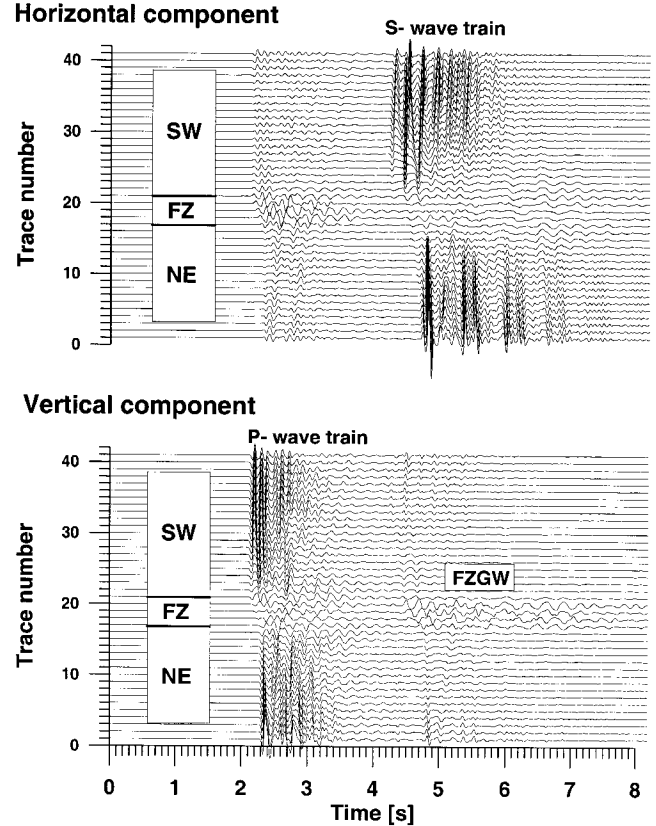
tion MMNB, separated by about 6 km. The figure illustrates two points. First, the model produces a good match to the observed FZGW-field characteristics. Second, the radically different FZGW amplitude characteristics for the source-receiver paths that propagate through the zone of high FZGW Q contrast significantly with those that do not cross through it.

Discussion

In this study, we characterized the amplitude information to image FZ structure for two reasons. First, travel-time tomography of FZGWs is difficult because there is a large uncertainty associated with picking of FZGW arrival times due to their dispersive nature and low frequency content. Second, the amplitudes of seismic waves generally reveal much stronger changes than travel times (up to several orders of magnitude) due to their greater sensitivity to material property variations compared to seismic velocities (where
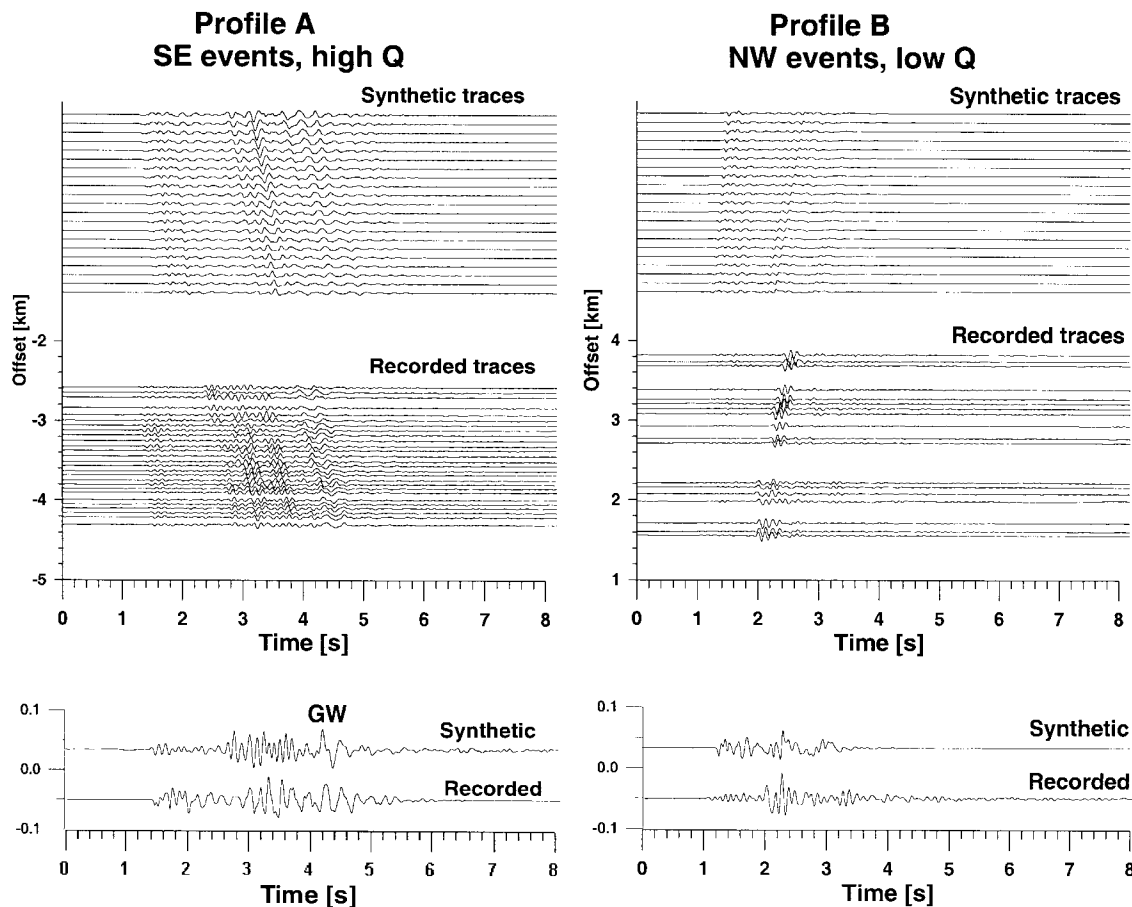
Figure 7. Comparison of synthetic and observed seismograms for two groups of traces recorded at MMNB, depicted as profiles A and B in Figures 2 and 4. This illustrates the striking difference in FZGW characteristics for propagation paths through the presumed high-Q source region versus paths outside of the anomalous zone. The lowermost traces compare individual synthetic and observed (shown by arrows) seismograms within the profiles.

10% changes are usually considered significant). Although velocity variations within wave guides affect both the amplitudes and travel times of guided waves, they can not explain the observed strong amplitude changes.

In Figure 8 we compare the spatial correlation of our FZGW attenuation image and its Q equivalent with other geophysical observations made along this segment of the SAF. The FZGW images show a relatively confined region of low FZGW attenuation that is about 4 km wide within and along the fault and that trends downward toward the northwest at about 60° throughout the full 3- to 12-km depth range of seismicity at Parkfield. The low-attenuation, high-Q feature extends from a shallow zone of intense microearthquake activity southeast of MMNB and dips steeply to the northwest through the rupture zones of the M 4.2, M 4.6, M 4.7, and M 5.0 events of 1992–1994, through the 1966 M 6 hypocenter, and into a group of deep aftershocks of the 1993 M 4.7 earthquake at 11–12 km depth. This dipping feature appears to separate the locked and creeping sections of the SAF at Parkfield as determined from geodetic data (Harris and

Segall, 1987) and as implied by a significant reduction in seismicity from the northwest to the southeast. It also coincides with a region of accelerated slip rate at depth that occurred in 1992–1994 as inferred by Nadeau and McEvilly (1999) from characteristic microearthquake recurrence rates. This feature also contains the region of anomalously low V_s and high V_p/V_s at depth observed by Michelini and McEvilly (1991). The shallow, most intense portion of the anomaly also lies beneath the zone that exhibits shallow travel-time changes reported in Vibroseis monitoring experiments (Karageorgi *et al.*, 1997; Korneev *et al.*, 2000).

While both the attenuation and Q images show the same gross features correlating to these additional observations, the Q image appears to provide greater localization of the locked-to-creeping boundary and a better match to the additional observations. The differences between the attenuation and Q images are due to the incorporation of the tomographic V_s model in generating the Q image. It seems surprising to find a decrease in V_s velocity in the region of high Q. But, as mentioned earlier, the V_s model represents
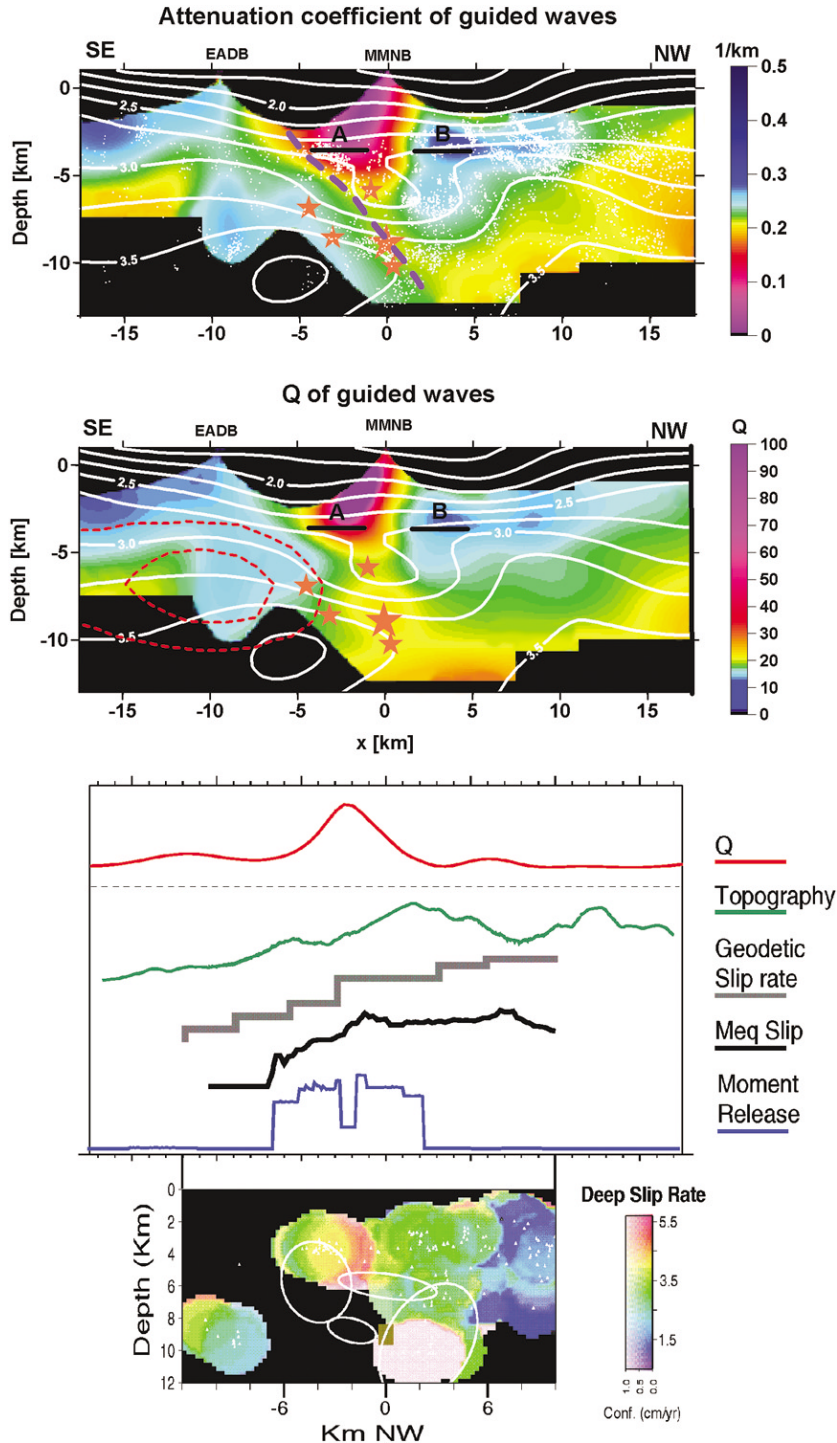
Figure 8. Spatial relationship of the FZGW attenuation/Q anomaly with other observations along the Parkfield segment of the SAF zone. The top two panels show in-fault attenuation and Q images resulting from the FZGW tomographic reconstructions. Note the zone of low FZGW attenuation (high Q) in the central portion of the panels delineating the transition at depth of locked to creeping fault (the purple dashed line is our interpretation of the locked-creeping boundary at depth). Also shown are V_s contours, 1987–1998 seismicity (white dots and small red stars for the four recent $M > 4$ events), and the 1966 M 6 hypocenter (large red star). The interseismic slip rate distribution by Harris and Segall (1987) is shown in thick dashed red contour lines on the top of Q image. The third panel shows the function of FZGW Q taken along a profile at 3.5 km depth. Shown immediately below the Q curve are curves representing topography along the fault (green), surface fault slip rates from geodetic data (Harris and Segall [1987], in grey), slip rates in the depth range 0–5 km inferred from recurrence intervals of characteristic microearthquake sequences (black), and the 1987–1998 moment release along the fault from southeast to northwest (blue). The bottom panel shows the along-fault deep slip rate distribution at Parkfield inferred from the recurrence times of characteristic microearthquakes occurring between mid-1992 and 1995 (inclusive; see Nadeau and McEvilly, 1999), and the aftershock regions of the $M > 4$ earthquakes occurring during this time period. Along-fault features in all these characteristics correlate spatially and appear to delineate the same transition from locked to creeping behavior on the surface and at depth on the SAF at Parkfield

an average velocity over the region between node points (1.2-km spacing) in the V_s tomographic inversion of the FZ and therefore does not provide a completely accurate picture of the true V_s structure inside the fault core. Velocity variations within the FZ most likely can be attributed to changes in fracture density and preferential orientation. While in the thin center FZ cores fractures are mostly oriented parallel to the fault plane, their orientation becomes orthogonal to the fault outside of the cores (Chester *et al.*, 1993). Incorporation

of V_s for the Q image is expected to provide a more accurate picture of the FZ structure than the attenuation image. It also suggests that given an even more detailed V_s model, a narrowing of the locked-creeping boundary zone should result. While the attenuation image provides a less detailed picture of the fault core structure, it is independent of any uncertainties associated with the distribution of V_s variations occurring within the node spacing of the V_s model.

Below the attenuation and Q panels we show a plot of

the Q function computed at a depth of 4 km and curves of other geophysical measurements taken along this segment of the SAF zone at Parkfield. These other curves include topographic elevation, fault-slip rates determined both geodetically at the surface (Harris and Segall, 1987) and at depth (1–5 km) inferred from characteristically repeating microearthquakes (Nadeau and McEvilly, 1999), and seismic moment release. We hypothesize that the transition in topography results from the evolution of gradual nonelastic vertical deformation resulting from repeated cycles of long-term stress accumulation concentrated at the transition from locked to creeping fault on this portion of the SAF. This interpretation is in agreement with drilling results, which suggest that the ridge at Middle Mountain is a pressure ridge, resulting from a localized overpressured zone beneath it. The data curves all exhibit good correlation with the along-fault features of the FZGW images. The bottom panel shows the along-fault deep slip rate distribution at Parkfield inferred from the recurrence times of characteristic microearthquakes occurring between mid-1992 and 1995 (inclusive; see Nadeau and McEvilly, 1999), and the aftershock regions of the $M > 4$ earthquakes occurring during this time period. It reveals a strong correspondence at all depths between the anomalous zone of FZGW propagation and the high slip-rate transient of 92–97. The dramatic changes in all these characteristics appears to correspond to a transition from locked to creeping behavior on the SAF at depth.

The cumulative evidence, then, suggests a special pathology in FZ dynamics associated with the FZGW low-attenuation region. We propose that (1) in combination these images and curves delineate, in detail and at depth, the likely northwest edge of the large locked asperity that periodically ruptures in recurring M 6 earthquakes at Parkfield and (2) FZGW propagation is directly affected by long-term evolving conditions in FZ material properties and by processes associated with strain accumulation and release.

The specific physical mechanisms responsible for the observed variations in seismic attenuation within the FZ are still unknown. We hypothesize that they are associated with fracture closure and opening due to changes in loading stress and nonelastic deformation. Laboratory data of time-lapse seismic attenuation measurements for fractured rocks during increasing normal load (Sobolev *et al.*, 1996) show a steady increase of Q, reaching a maximum value shortly before rock failure. The spatial distribution of Q for the SAF at Parkfield appears to exhibit similar behavior if the FZ rocks are being stressed toward failure along the locked-creeping boundary, as expected at the edge of earthquake-prone zone southeast of the Q anomaly. The process of fracture opening and development also involves dewatering of rocks and water pressure changes. If such processes are occurring in deep FZs, it suggests the potential for monitoring of stress changes in FZ cores using guided waves. A greater understanding of the relationships between the attenuation of FZGWs, fluid and fracturing processes, stress accumulation, and the occurrence of earthquakes is needed to obtain a clearer picture of the physics of earthquake occurrence and the viability of using FZGWs to provide useful precursory information on earthquake-prone faults.

Conclusions

We have developed a method of multisource processing using Parkfield microearthquakes distributed along the inner FZ and recorded at the only two borehole HRSN stations close to the SAF to create a robust tomographic inversion of FZGW attenuation. The inversion provides a detailed 2D image of FZ structure along a 35-km segment of the SAF at depth. Waveform modeling indicates the width of a narrowly defined (200 $\pm$ 30)-m-wide low-velocity SAF fault core at Parkfield.

Using our FZGW attenuation images and waveform modeling, we have identified an anomalous zone of low FZGW attenuation in a region postulated to delimit the deep locked and creeping segments on the SAF. This zone correlates with and may be responsible for a number of independently observed phenomena, including slip-rate transients at depth, the occurrence of four $M > 4$ earthquakes occurring during the slip transient period, and shallow seismic velocity changes seen using Vibroseis. We propose that the anomalous feature is a locus of high stress or deformational strain concentration along the northwest-dipping edge of the M 6 asperity at Parkfield. Suggested mechanisms for explaining the relatively high Q in the fault core at Parkfield involve long-term processes of nonelastic deformation, fracture closure or compression of the material within the fault core, dewatering, fault-normal compression, and changes in fracture orientation due to the evolution of a complex stress field at this transitional zone of the SAF.

Our results also demonstrate the potential of similar FZGW studies for imaging and understanding the structure and properties of inner regions of FZs. Since FZGWs primarily propagate in the low-velocity core region of FZs, they sample the most active zone of fault deformation and provide greater structural detail of the inner fault core than body waves, which propagate primarily outside of the central core region.

Further knowledge of the physics responsible for FZGW propagation promises to provide clues to the material rock properties, processes, and geometry of FZs at depth. FZGW studies may also provide a valuable tool for delineating locked fault segment boundaries, for establishing the continuity and extent of fault segments, and for monitoring ongoing fault processes resulting from stress accumulation. With an increased number of stations located in or near FZ cores, FZGW inversion can provide further detail on changing conditions in the nucleation zones of large earthquakes, as stress accumulates on their associated locked boundaries.

Acknowledgments

References

Ben-Zion, Y. (1998). Properties of seismic fault zone waves and their utility for imaging low velocity structures, *J. Geophs. Res.* **103,** 12,567–12,585.

Ben-Zion, Y., and K. Aki (1991). Seismic radiation from an *SH* line source in a laterally heterogeneous planar fault zone, *Bull. Seism. Soc. Am.* **80,** 971–994.

Ben-Zion, Y., and P. Malin (1991). San Andreas fault zone hEADB waves near Parkfield, California, *Science* **251,** 1592–1594.

Chester, F. M., J. P. Evans, and R. L. Biegel (1993). Internal structure and weakening mechanisms of the San Andreas Fault, *J. Geophs. Res.* **98,** 771–786.

Feng, R., and T. V. McEvilly (1983). Interpretation of seismic reflection profiling data for the structure of the San Andreas fault zone, *Bull. Seism. Soc. Am.* **73,** 1701–1720.

Harris, R. A., and P. Segall (1987). Detection of a locked zone at depth on the Parkfield, California, segment of the San Andreas Fault, *J. Geophs. Res.* **92,** 7945–7962.

Igel, H., Y. Ben-Zion, and P. C. Leary (1997). Simulation of *SH*- and *P-SV*-wave propagation in fault zones, *Geophys. J. Int.* **128,** 533–546.

Karageorgi, E., R. Clymer, and T. V. McEvilly (1992). Seismological studies at Parkfield. II. Search for temporal variations in wave propagation using Vibroseis, *Bull. Seism. Soc. Am.* **82,** 1388–1415.

Karageorgi, E. D., T. V. McEvilly, and R. W. Clymer (1997). Seismological studies at Parkfield. IV. Variations in controlled-source waveform parameters and their correlation with seismic activity, 1987–1994, *Bull. Seism. Soc. Am.* **87,** 39–49.

Korneev, V. A., T. V. McEvilly, and E. D. Karageorgi (2000). Seismological studies at Parkfield. VIII. Modeling the observed controlled-source waveform changes, *Bull. Seism. Soc. Am.* **90,** 702–708.

Leary, P. C., Y.-G. Li, and K. Aki (1985). Borehole observations of fault zone trapped waves, Oroville, CA, *EOS* **66,** 976.

Li, Y. G., K. Aki, J. E. Vidale, and F. Xu (1999). Shallow structure of the Landers fault zone using explosion-excited trapped waves, *J. Geophys. Res.* **104,** no. B6, 20,257–20,275.

Li, Y.-G., W. L. Ellsworth, C. H. Thurber, P. E. Malin, and K. Aki (1997). Fault-zone guided waves from explosions in the San Andreas fault at Parkfield and Cienega valley, California, *Bull. Seism. Soc. Am.* **87,** 210–221.

Li, Y.-G., P. C. Leary, K. Aki, and P. E. Malin (1990). Seismic trapped modes in the Oroville and San Andreas fault zones, *Science* **249,** 763–766.

Li, Y.-G., J. E. Vidale, K. Aki, C. Marone, and W. H. K. Lee (1994). Fine structure of the Landers fault zone: segmentation and the rupture process, *Science* **265,** 367–370.

Li, Y.-G., J. E. Vidale, K. Aki, F. Xu, and T. Burdette (1998). Evidence of shallow fault zone strengthening after the 1992 *M* 7.5 Landers, California, earthquake, *Science* **279,** 217–219.

Michelini, A., and T. V. McEvilly (1991). Seismological studies at Parkfield. I. Simultaneous inversion for velocity structure and hypocenters using B-splines parameterization, *Bull. Seism. Soc. Am.* **81,** 524–552.

Nadeau, R. M., and L. R. Johnson (1998). Seismological studies at Parkfield. VI. Moment release rates and estimates of source parameters for small repeating earthquakes, *Bull. Seism. Soc. Am.* **88,** 790–814.

Nadeau, R. M., and T. V. McEvilly (1997). Seismological studies at Parkfield. V. Characteristic microearthquake sequences as fault-zone drilling targets, *Bull. Seism. Soc. Am.* **87,** 1463–1472.

Nadeau, R. M., and T. V. McEvilly (1999). Fault slip rates at depth from recurrence intervals of repeating microearthquakes, *Science* **285,** 718–721.

Nadeau, R. M., M. Antolik, W. Foxall, P. A. Johnson, and T. V. McEvilly (1994). Seismological studies at Parkfield. III. Microearthquake clusters in the study of fault-zone dynamics, *Bull. Seism. Soc. Am.* **84,** 247–263.

Nadeau, R. M., W. Foxall, and T. V. McEvilly (1995). Periodic recurrence and spatial clustering in characteristic microearthquakes on the San Andreas fault, *Science* **267,** 503–507.

Sobolev, G. A., O. V. Babichev, V. F. Los, A. V. Kol'tsov, A. V. Ponomaryov, V. I. Ponyatovskaya, A. S. Rozanov, S. A. Stanchits, A. A. Khromov, D. I. Frolov, L. Yangquan, Z. Jialiu, Q. Jiadong, and L. Shiyu (1996). Precursors of the destruction of water containing blocks of rock, *J. Earthquake Pred. Res.* **5,** 63–91.

Appendix A

Consider the model describing the amplitude of guided waves from equation (1),

$$U_{ij} = A_j M_i \frac{\kappa(\theta_{ij})}{\sqrt{r_{ij}}} \exp(- \sum_n \alpha_n r_{ijn}), \qquad (A1)$$

where the same notations are used. The amplitude of a direct *S*-wave recorded for the same event is

$$U_{ij}^S = A_{Sj} M_i \frac{\kappa(\theta_{ij})}{r_{ij}}, \qquad (A2)$$

where we assume attenuation inside the FZ is negligibly smaller than outside of it. We then have the ratio

$$U_{ij}/U_{ij}^S = \bar{A}_j \sqrt{r_{ij}} \exp(- \sum_n \alpha_n r_{ijn}), \quad \bar{A}_j \equiv A_j/A_{Sj}. \qquad (A3)$$

Next we solve equation (A3) in two stages. First, after taking the logarithm of the data

$$u_{ij} = a_j - \sum_n \alpha_n r_{ijn}, \quad u_{ij} \equiv \ln(U_{ij}/U_{ij}^S/\sqrt{r_{ij}}), \quad a_j \equiv \ln \bar{A}_j, \qquad (A4)$$

we find the least-square solution estimates for a_j and α_0, assuming a constant background value of $\alpha_n = \alpha_0$. Substituting these estimates into equation (A4) we get

$$\hat{a}_j - \sum_n \Delta\alpha_n r_{ijn} - u_{ij} = \sum_n \Delta\alpha_n r_{ijn}, \quad \Delta\alpha_n \equiv \alpha_n - \alpha_0. \qquad (A5)$$

Finally we use the method of algebraic reconstruction and invert equation (A5) for the unknown residual attenuations. $\Delta\alpha_n$.

Center for Computational Seismology
Earth Sciences Division
Lawrence Berkeley National Laboratory
Berkeley, California 94720
  (V.A.K.)

Berkeley Seismological Laboratory
University of California
Berkeley, California 94720
  (R.M.N., T.V.M.)